



1        **Correcting for trace gas absorption when retrieving aerosol optical**  
2        **depth from satellite observations of reflected shortwave radiation**

3                    Falguni Patadia<sup>1,2</sup>, Robert C. Levy<sup>2</sup>, Shana Mattoo<sup>2,3</sup>

4        <sup>1</sup>GESTAR/Morgan State University, Columbia, MD, USA

5        <sup>2</sup>NASA Goddard Space Flight Center, Greenbelt, MD, USA

6        <sup>3</sup>SSAI, Lanham, MD, USA

7

8



## 9 Abstract

10 Retrieving aerosol optical depth (AOD) from top-of-atmosphere (TOA) satellite-  
11 measured radiance requires separating the aerosol signal from the total observed signal. Total  
12 TOA radiance includes signal from underlying surface and from atmospheric constituents such  
13 as aerosols, clouds and gases. Multispectral retrieval algorithms, such as the dark-target (DT)  
14 algorithm that operates upon Moderate Resolution Imaging Spectroradiometer (MODIS,  
15 onboard Terra and Aqua satellites) and Visible Infrared Imaging Radiometer Suite (VIIRS,  
16 onboard Suomi-NPP) sensors, use wavelength bands in “window” regions. However, while  
17 small, the gas absorptions in these bands are non-negligible and require correction. In this paper  
18 we use High-resolution TRANsmiission (HITRAN) database and Line-by-Line Radiative  
19 Transfer Model (LBLRTM) to derive consistent gas corrections for both MODIS and VIIRS  
20 wavelength bands. Absorptions from H<sub>2</sub>O, CO<sub>2</sub> and O<sub>3</sub> are considered, as well as other trace  
21 gases. Even though MODIS and VIIRS bands are “similar”, they are different enough that  
22 applying MODIS specific gas corrections to VIIRS observations results in an underestimate of  
23 global mean AOD (by 0.01), but with much larger regional AOD biases up to 0.07. As recent  
24 studies are attempting to create a long-term data record by joining multiple satellite datasets,  
25 including MODIS and VIIRS, the consistency of gas correction becomes even more crucial.  
26



27           **1. Introduction**

28           Aerosols are tiny particles in the atmosphere that scatter and/or absorb incoming solar  
29 insolation, and because of this are active players in Earth's energy budget [*IPCC*, 2013]. In  
30 addition aerosols affect cloud and precipitation processes [*Denman et al.*, 2007; *Boucher et al.*,  
31 2013], and they degrade air quality, contributing to increased morbidity and mortality rates  
32 world-wide [*Lim et al.* 2012]. For these reasons characterizing and monitoring aerosol  
33 distributions has become a global priority [*Boucher et al.*, 2013].

34           Satellite aerosol remote sensing allows for characterization and monitoring of aerosols  
35 over broad regions and globally [*Lenoble et al.*, 2013]. Different aerosol remote sensing  
36 schemes are applied, depending on the information received by the different satellite sensors  
37 [*McCormick et al.*, 1979; *Herman et al.*, 1997; *Stowe et al.*, 1997; *Tanré et al.*, 1997; *Kaufman et*  
38 *al.*, 1997a; *Torres et al.*, 1998; *Veefkind et al.*, 1998; *Higurashi and Nakajima*, 1999; *Deuzé et*  
39 *al.*, 1999; *Knapp et al.*, 2002; *Martonchik et al.*, 1998; *Liu et al.*, 2005; *Kahn et al.*, 2001]. In  
40 terms of passive satellite sensors that measure solar radiation reflected by the Earth-atmosphere  
41 system, aerosol remote sensing methods must isolate the information obtained from the solar  
42 radiation interacting with suspended aerosol particles from the information obtained from all  
43 other interactions: reflectance from the surface, scattering from atmospheric molecules and  
44 clouds, absorption by atmospheric gases, etc. [*Vermote et al.*, 1997]. Thus, characterizing and  
45 removing these other sources of information in the satellite signal becomes a fundamental part of  
46 the process.

47           Some of the interactions requiring removal continue to receive considerable attention as  
48 new sensors are deployed and new aerosol remote sensing algorithms are derived. These include  
49 characterizing the contribution from the surface and masking clouds [*Hutchison et al.*, 2008; *Shi*



50 *et al.*, 2014;]. Other interactions received much less attention, as these are considered to be well-  
51 understood and simple to apply in new situations. These latter include molecular scattering and  
52 gaseous absorption [Tanré *et al.*, 1992; Vermote *et al.*, 1997]. However, the requirements on  
53 accuracy of aerosol remote sensing products become tighter as instrument capabilities,  
54 calibration and retrieval methods improve. For example, Hollman *et al.*, (2013) has recently  
55 suggested that for reducing uncertainties on climate, aerosol optical depth (AOD) should be  
56 monitored to an accuracy on the order of  $\pm(0.03 + 10\%$ ; e.g. GCOS, 2011). The Atmospheric  
57 Clouds and ocean Ecosystems (ACE) white paper called for an accuracy of  $\pm(0.02 + 10\%)$  [Starr  
58 *et al.*, 2010]. To meet such tight criteria, all aspects of traditional aerosol remote sensing  
59 methods require re-examination with the objective to reduce uncertainties in the final retrieval,  
60 and to assure continuity as the aerosol climate data record is passed from one sensor to the next.

61 In this paper we focus on gaseous absorption. Aerosol retrieval algorithms (Vermote *et*  
62 *al.*, 1997) tend to use satellite observations taken in wavelength regions where gas absorptions  
63 are small. However, while gas absorption is small in these “window” bands, it is not zero. For  
64 example, for the 20 nm-wide Moderate Resolution Imaging Spectroradiometer (MODIS) band  
65 near 0.55  $\mu\text{m}$ , in the middle of the Chappius region, there is absorption due to ozone. For a US  
66 1976 Standard Atmosphere (US76, 1976), with total column ozone of 344 Dobson Units (DU),  
67 the gas absorption optical depth ( $\tau^{\text{GAS}}$ ) is about 0.03 in this band. This is of similar magnitude as  
68 pristine AOD ( $\sim 0.05$ ), and equal to the required measurement accuracy (GCOS; 2011). Water  
69 vapor, measured as precipitable water vapor (PW or  $w$ ), absorbs as well and introduces even  
70 greater uncertainty. For example, the  $w$  of the US76 standard atmosphere is a modest 1.4 cm,  
71 which translates to  $\tau^{\text{GAS}}$  of about 0.025 in the MODIS 2.11  $\mu\text{m}$  band or a  $\tau^{\text{GAS}}$  of 0.05 for a  
72 similar-wavelength Visible Infrared Imaging Radiometer Suite (VIIRS) band centered near 2.25



73  $\mu\text{m}$ . The major difficulty with ozone and water vapor is that the total column burden of these  
74 gases varies spatially and temporally over the globe [Hegglin *et al.*, 2014]. Other trace gases,  
75 including carbon dioxide and methane, also absorb shortwave radiation in wavelength specific  
76 regions. While these gases are more evenly distributed (well-mixed) throughout the globe, failing  
77 to correct for their absorption also would lead to errors in aerosol retrieval.

78 Different aerosol retrieval algorithms respond to the challenge of gaseous correction  
79 differently. Some include all gaseous absorbers and account for the variability of water vapor  
80 and ozone [Levy *et al.*, 2013; 2015], while others use a fixed ozone concentration [e.g Thomas *et*  
81 *al.*, 2010; Sayer *et al.*, 2012], and others correct for some gases, but consider the effect of other  
82 gases to be too small to bother with [MISR ATBD]. Few include methane [Levy *et al.*, 2013;  
83 2015]. How does a less complete gaseous correction scheme affect the global retrieval of AOD?  
84 How sensitive are gaseous absorption schemes to slight shifts in spectral bands from instrument  
85 to instrument? While all operational aerosol retrieval algorithms employ gaseous correction  
86 schemes in their retrieval and describe these schemes, more or less, within the “gray literature”  
87 of internal documentation, there are few recent articles in the peer-reviewed literature that openly  
88 describe the process and quantify the impact of the subtle choices made during algorithm  
89 development.

90 In this paper we re-examine gaseous correction as it is applied in the traditional MODIS  
91 Dark Target (DT) aerosol retrieval [Levy *et al.*, 2013], and as that retrieval algorithm is ported to  
92 the new VIIRS data [Levy *et al.*, 2015]. In Section 2 we discuss the absorption of radiation by  
93 atmospheric gases within the MODIS and VIIRS bands used for the DT aerosol retrieval. We  
94 introduce the relationship of gas abundance to its transmittance spectra, which is the theoretical  
95 basis for gas corrections in DT AOD retrievals. The atmospheric correction methodology is



96 detailed in Section 3. The impact of the updated atmospheric gas corrections applied to the  
97 Collection 6 MODIS AOD is also briefed in Section 3. In Section 4 we discuss the importance of  
98 accurate atmospheric gas corrections in context of DT AOD retrievals from the VIIRS  
99 instrument. The study is summarized and concluded in Section 5.

100

## 101 **2. The DT approach to aerosol retrieval and gas correction**

### 102 **2.1 The DT aerosol algorithm and wavelength bands**

103 As explained in detail by Levy et al. (2013; 2015) and references therein, the dark-target  
104 (DT) aerosol algorithm uses seven channels (or bands) covering the solar reflective spectral  
105 region from blue through the shortwave infrared (SWIR) to characterize aerosols, clouds and  
106 Earth's surface. These bands were specifically chosen to correspond to the spectral window  
107 regions of minimal gas absorption. On MODIS, these bands include B1, B2, B3, B4, B5, B6 and  
108 B7, which are each 20-50 nm in width and centered near 0.65, 0.86, 0.47, 0.55, 1.24, 1.63 and  
109 2.11  $\mu\text{m}$ , respectively. On VIIRS, the DT algorithm uses bands M3, M4, M5, M7, M8, M10 and  
110 M11, which are the "moderate resolution" or M-bands that are centered near 0.48, 0.55, 0.67,  
111 0.86, 1.24, 1.60 and 2.26  $\mu\text{m}$ , respectively.

112 The DT algorithm is actually two algorithms, one applied to MODIS- or VIIRS-measured  
113 reflectance over land surfaces and the other to measured reflectance over ocean (Levy et al.,  
114 2013; 2015). Both the land/ocean algorithms employ a single atmospheric gas correction method  
115 before any retrieval is performed. DT uses a LUT approach in which atmospherically corrected  
116 observed top-of-atmosphere (TOA) reflectance (as measured by the satellite) is compared with  
117 simulated reflectance. The simulations are calculated by radiative transfer codes, and account for



118 multiple scattering and absorption effects of a combined surface (land or water), molecular  
119 (Rayleigh), and aerosol scene, but do not account for gaseous absorption. These simulations also  
120 account for the angular dependence of the scattered radiation, through use of a pseudo-spherical  
121 approximation (e.g. Ahmad and Fraser, 1991). The DT retrieval operates on regions of pixels for  
122 which cloud pixels, glint pixels, and other unsuitable pixels have been masked out. Thus, the DT  
123 aerosol retrieval is performed for cloud-free sky, and assumptions have been made for the  
124 surface reflectance properties and atmospheric constituents. The LUT is interpolated as a  
125 function of observing geometry (solar and view zenith and azimuth angles), and then searched to  
126 determine which aerosol conditions provide spectral reflectance that best “matches” the spectral  
127 reflectance observed by the satellite. The reported solution (retrieved spectral AOD) is some  
128 function of the solutions that meet sufficient criteria for matching the observations. For the DT  
129 algorithm, expected uncertainty for retrieved AOD at  $0.55 \mu\text{m}$  (as compared to global network of  
130 sun photometers) is  $\pm(0.05 + 15\%)$  over land, and  $\pm(0.03 + 10\%)$  over ocean [Levy *et al.*, 2013].

131         These LUTs are created as if the atmosphere is composed only of aerosol and scattering  
132 (Rayleigh) molecules. The gas absorption is assumed to be zero. This is because of the large  
133 spatial/seasonal variability of two of the primary absorbers: ozone and water vapor. Ozone can  
134 range from 100 to 500 DU around the globe [Hegglin *et al.* 2014] and water vapor varies by an  
135 order of magnitude from the wet tropics to the dry poles. It would be cumbersome and  
136 computationally inefficient to add two or more new indices to the LUT and cover the dynamic  
137 range of each gas in the LUT calculation.

138         While gas absorption in these window bands may be small, they are not zero, as  
139 described above. Figure 1 shows the TOA transmission spectra (black lines) in the  $0.4 - 2.5 \mu\text{m}$



140 spectral range in the presence of major gases, including H<sub>2</sub>O, O<sub>3</sub>, CO<sub>2</sub>, CH<sub>4</sub>, O<sub>2</sub>, N<sub>2</sub>O, and CO.  
141 The transmission spectra of each gas were calculated using the Line-by-Line Radiative Transfer  
142 Model (LBLRTM) code [Clough *et al.*, 1992, 2005] for a nadir viewing geometry and for the US  
143 1976 Standard Atmosphere (US76; 1976). A transmittance of 1.0 indicates that the atmosphere  
144 is transparent to incoming solar radiation (insolation) i.e. it is not absorbed in the atmosphere.  
145 Overlaid on Fig. 1 are the spectral response functions of the seven MODIS channels (blue  
146 curves) and seven VIIRS channels (red curves) used in the DT retrievals. As can be seen from  
147 Fig. 1, depending on the wavelength, the atmosphere can be totally transparent to a certain gas  
148 and partially opaque to another. For example, in the MODIS 0.62-0.67  $\mu\text{m}$  band (B1), H<sub>2</sub>O, O<sub>3</sub>,  
149 and O<sub>2</sub>, absorb radiation while CO<sub>2</sub>, N<sub>2</sub>O, CO, and CH<sub>4</sub> do not. In the 1.230 – 1.250  $\mu\text{m}$  band  
150 (B5), O<sub>2</sub>, H<sub>2</sub>O and CO<sub>2</sub> are major absorbers while other gases are not. Absorption bands of the  
151 major atmospheric gases are listed in Table 1.

152 Note that there are also wavelength regions that are nearly opaque because of gas  
153 absorption. For example, Fig. 1 shows the well-known water vapor absorption within the  
154 wavelength region near 1.38  $\mu\text{m}$ . Because of the strong absorption, the 1.38  $\mu\text{m}$  band cannot be  
155 used for aerosol retrieval. Yet, this band is very useful for detecting cirrus clouds that would  
156 otherwise contaminate a cloud-free aerosol retrieval (Gao *et al.*, 2002). This special case of using  
157 absorption information is not discussed further in this paper.

## 158 **2.2 Derivation of a gas absorption correction**

159 Because the LUT is calculated without gas absorption, an alternative technique must be  
160 substituted to account for the effect of the gases in each wavelength. If not, then when the  
161 algorithm attempts to match the measured TOA reflectances to the LUT-calculated reflectances





162 the LUT values will be brighter than the measured values for the same amount of aerosol. In the  
163 most straightforward sense retrieved AOD, dominated by scattering, will be systematically too  
164 low because the retrieval will be searching for a less bright TOA reflectance in the LUT, with  
165 less aerosol, to match the observed values. The algorithm deals with this mismatch between  
166 measured and LUT reflectance caused by the missing gas absorption in the LUT values by  
167 adjusting *the measured* TOA reflectances in each wavelength band, in effect brightening the  
168 measurements to better match the values in the LUT.

169 Figure 1 shows that five gases (H<sub>2</sub>O, O<sub>3</sub>, CO<sub>2</sub>, O<sub>2</sub> and CH<sub>4</sub>) have absorption lines that fall  
170 within the wavelength bands used for the DT aerosol retrieval. Because each window band spans  
171 tens of nanometers, every DT channel is affected by at least one gas where the transmittance is  
172 less than 1.0.

173 We have introduced two measures, gas opacity and transmissivity corresponding to the  
174 gas absorption optical depth and transmittance. The two parameters are related via,

$$T_{\lambda}^i = \exp(-G^i \tau_{\lambda}^i) \quad \dots \dots \dots (1)$$

175  
176 where  $T_{\lambda}^i$  is the downward transmittance for a particular wavelength band or  $\lambda$ , and for a  
177 particular absorbing gas “ $i$ ”, and where  $\tau_{\lambda}^i$  is the gas optical depth designated for the particular  
178 gas and wavelength and  $G^i$  is the airmass factor (slant path through the atmosphere) for gas  $i$ .  
179 Equation (1) shows that transmission of light is a function of the atmospheric path length ( $G^i$ )  
180 and the gas optical depth ( $\tau_{\lambda}^i$ ), and that transmissivity decreases with increasing air mass and  
181 increasing gas concentration.

182

### 183 2.2.1 Gas optical depth



184 The gas optical depth,  $\tau_{\lambda}^i$ , represents the spectral integral over the wavelength band, and  
185 if the gas concentration was uniform along the path (column), then  $\tau_{\lambda}^i$  would be directly  
186 proportional to the loading of gas  $i$  in the column. Some gases are indeed well-mixed in the  
187 atmosphere, but water vapor and ozone are not. These important absorbers exhibit distinctive  
188 vertical profiles, as will be discussed in Section 3.1. Note that each individual gas has its own  
189 particular absorption efficiency based on its characteristic absorption cross section, and that for  
190 the same column concentrations  $\tau_{\lambda}^i$  will be different for different gases. In the absence of a long  
191 slant path, and for small gas optical depths ( $\tau_{\lambda}^i \ll 1.0$ ), transmission can be estimated by  $T_{\lambda}^i \sim 1 -$   
192  $G^i \tau_{\lambda}^i$ .

193

### 194 2.2.2 Airmass factor

195 The airmass factor,  $G$  can be approximated as  $G=1/\cos Z$  where  $Z$  is the zenith angle, for a  
196 homogenous (exponential decay) atmosphere, and for small values (near nadir) of a zenith angles  
197  $Z$ . This is the flat earth approximation. As  $Z$  increases beyond  $60^\circ$ , the air mass factor is more  
198 accurately described by spherical shell geometry towards the horizon [Gueymard, 1995], i.e.:

$$G = \sqrt{(r \cos Z)^2 + 2r + 1} - r \cos Z \quad \dots \dots \dots (2)$$

199 where,  $r = R_E / H_{atm}$ ;  $R_E$  = radius of Earth (6371km) and  $H_{atm}$  = effective scale height of the  
200 atmosphere (approx 9km). This expression accounts for Earth's sphericity and atmospheric  
201 refraction. Differences in computing  $G$  are small for  $Z < 70^\circ$ , but increase to 10% as  $Z = 84^\circ$  (the  
202 maximum zenith angle allowed within the DT algorithm).

203 Yet, there are complications. When atmospheric constituents are well-mixed and their  
204 concentrations are nearly proportional to altitude within the atmosphere, Eq (2) is sufficient.  
205 However, water vapor (concentrated near the surface) and ozone (concentrated in the



206 stratosphere) are not well-mixed in the vertical, having different scale heights. In this layered  
 207 situation (rather than continuous), there are empirical formulas (e.g. *Kasten and Young*, 1989)  
 208 that provide slight improvements to the calculation of G assuming spherical geometry. For  
 209 example, *Gueymard*, [1995] derived the empirical formula

$$G^i = (\cos Z + a_{i,1}Z^{a_{i,2}} * (a_{i,3} - Z)^{a_{i,4}})^{-1} \quad \dots \dots \dots (3)$$

210 where  $a_{i,j}$  are coefficients ( $j=1,4$ ) for gas type  $i$ . Thus,  $G^i$  varies with gas type and specific profile  
 211 within the atmosphere. The values of coefficients  $a_{i,j}$  can be found in Table 4.1 of *Gueymard*,  
 212 [1995].

213 As long as the total gas optical depth is small ( $\sum_i \tau_\lambda^i \ll 1.0$ ), the total transmission of all  
 214 trace gases is well-approximated by the product of each individual gas (i.e.):

$$T_\lambda^{GAS} = \prod_i T_\lambda^i = \exp\left(\sum_i -G^i \tau_\lambda^i\right) \quad \dots \dots \dots (4a)$$

215 The total gas transmissivity defined in Equation (4a) for each wavelength band quantifies the  
 216 degree to which the measured reflectance will be diminished due to gaseous absorption. In order  
 217 to match the measured reflectances to those calculated for the LUT, these diminished  
 218 reflectances have to be “corrected” or brightened. This correction factor is simply the inverse  
 219 transmissivity,  $\tilde{T}$ ,

$$\tilde{T}_\lambda^{GAS} = 1/T_\lambda^{GAS} = \exp\left(\sum_i G^i \tau_\lambda^i\right), \quad \dots \dots \dots (4b)$$

220 which when multiplied with the measured reflectance restores the amount of light absorbed by  
 221 gases along the one-way path of transmission. Or, given a measured radiance,  $L_M$ , the corrected  
 222 (brightened) radiance  $L$ , is simply,  $L = L_M * \tilde{T}$ .



223           When observing from a ground-based sun photometer (e.g. AERONET), the correction is  
224 straightforward, because the path of transmission traverses the depth of the atmosphere only  
225 once. The problem is more complicated for satellite remote sensing, because a satellite measures  
226 radiation that has traveled downwards through the atmosphere and then back up to space. We  
227 have to calculate a two-way correction factor and  $G$  must account for the  $Z$  angles of both  
228 downward (the solar zenith angle) and upward paths (view zenith). As  $Z$  gets large, the vertical  
229 profile of the gas (layering) becomes more important.

230           There are two parameters determining the transmission,  $T_{\lambda}^{GAS}$ , and therefore the  
231 correction factor,  $\tilde{T}_{\lambda}^{GAS}$ , and these are  $G^i$  and  $\tau_{\lambda}^i$ . The goal, then, is to parameterize equation 4(a)  
232 or 4(b) i.e. the relationship between atmospheric transmission of gas and  $G^i\tau_{\lambda}^i$ ; taking into  
233 consideration the varying gas concentrations and their vertical profiles through the atmosphere,  
234 around the globe. Furthermore, the parameterization will be developed to link  $\tilde{T}_{\lambda}^{GAS}$  directly to  
235 column measures of the gases instead of to the optical depth. This allows the algorithm to  
236 bypass calculations of optical depth from inputs of precipitable water vapor ( $w$  in cm) and ozone  
237 ( $O$  in Du), and instead use the inputs directly.

238

### 239           **3. Use of LBLRTM to derive gas absorption parameterization**

240

241           To develop an empirical relationship between atmospheric gas transmission, the airmass  
242 factor ( $G^i$ ) and its optical depth ( $\tau_{\lambda}^i$ ), we require a radiative transfer (RT) code that can  
243 accurately simulate the gaseous absorption and transmission process in the atmosphere. Among  
244 other things, the RT code requires these two pieces of information: (a) the absorption cross-  
245 sections and concentration of gas constituent in spectral bands of interest and (b) accurate high-



246 resolution information of the absorption spectra of the relevant gases. The MODIS and/or VIIRS  
247 channels widths are on order of 20-50 nm. We require a high-resolution database to capture the  
248 fine absorption lines within these bandwidths. To address (a) and (b), we use the Line-By-Line  
249 Radiative Transfer Model (LBLRTM) to parameterize equations 4(a) and 4(b) instead of a  
250 MODTRAN based RT code. The following section provides details of LBLRTM.

251

### 252 3.1 LBLRTM description

253 The Line-By-Line Radiative Transfer Model (LBLRTM) is known to be an accurate and  
254 flexible radiative transfer model that can be used over the full spectral range from ultraviolet to  
255 microwave [Clough et al., 2005]. It uses the High-resolution TRANsmission (HITRAN)  
256 molecular absorption database [Rothman et al., 2009] for calculating transmittance and radiance  
257 of molecular species. The HITRAN2008 database contains over 2,713,000 lines for 39 different  
258 molecules. The spectral resolution of the data is different in different spectral regions and for  
259 different species [see Rothman et al., 2009]. For example, for water vapor absorption in the Near  
260 IR region, the line resolution is  $0.001 \text{ cm}^{-1}$  [2.5 – 3.4  $\mu\text{m}$ ]. The LBLRTM has been extensively  
261 validated against atmospheric radiance spectra [e.g. Turner et al., 2003; Shephard et al., 2009;  
262 Alvarado et al., 2013]. Use of the HITRAN database and other attributes of LBLRTM provide  
263 spectral radiance calculations with accuracies that are consistent with validation data. Limiting  
264 errors are, in general, attributable to line parameters and line shape. Algorithmic accuracy of  
265 LBLRTM is approximately 0.5% and is about five times less than the error associated with line  
266 parameters [Clough et al., 2005].

### 267 3.2 LBLRTM calculations for MODIS and VIIRS



268           The LBLRTM model was run for many scenarios representing different combinations of  
269 gas vertical profiles, gas concentrations and air mass factors for each type of gas and each of the  
270 wavelength bands of interest. Transmissions of the ten important atmospheric gases, viz. H<sub>2</sub>O,  
271 O<sub>3</sub>, O<sub>2</sub>, N<sub>2</sub>O, NO<sub>2</sub>, NO, SO<sub>2</sub>, CO<sub>2</sub>, CO, and CH<sub>4</sub>, that affect either the MODIS or the VIIRS  
272 spectral bands [Levy *et al.*, 2013] were calculated. The results link transmission,  $T_{\lambda}^i$ , or gas  
273 correction factor,  $\tilde{T}_{\lambda}^i$ , to gas path length,  $G_{H_2O}^w$  or  $G_{O_3}^O$ , for water vapor (H<sub>2</sub>O) and ozone (O<sub>3</sub>),  
274 respectively, where  $w$  is the precipitable water vapor in cm and  $O$  is ozone column loading in  
275 DU. Values for  $w$  and  $O$  are input into the algorithm from ancillary data. The other gases are  
276 considered to be well-mixed and not varying spatially or temporally, and therefore, are not  
277 dependent on input ancillary data. The final parameterization will be curve fits through the  
278 scatter of the model results.

279           As described in Section 2.2,  $\tilde{T}_{\lambda}^{GAS}$  will be affected by the vertical distribution of the gases  
280 in the column, especially at oblique zenith angles. To account for this effect in building the  
281 parameterization we use 52 atmospheric profiles (personal communication, Pubu Ciren, NOAA)  
282 that were obtained from model runs, and characterize different locations and seasons (Figure 2).  
283 The columnar gas concentrations differ across the 52 profiles, varying by more than a factor of  
284 ten for water vapor, and by 100% for ozone. Except for NO<sub>2</sub>, which is highly variable in both  
285 horizontal and vertical, the other trace gases tend to be well-mixed throughout the atmosphere.  
286 Using radiative transfer calculations, Ahmad *et al.*, (2007) show that NO<sub>2</sub> has largest impact  
287 (1%) on TOA reflectance in the blue channels (412 and 443 nm). Other visible channels are  
288 impacted to a lesser degree. We will use the term ‘dry gas’ to denote the eight gases that are  
289 neither H<sub>2</sub>O or O<sub>3</sub>, and use the US 1976 Standard Atmosphere (US 76) as a default profile.



290 For H<sub>2</sub>O and O<sub>3</sub>, and each of their respective profiles, we use LBLRTM to calculate air  
291 mass factors and transmissions for 10 values of viewing zenith angle, ranging from 0° – 80°.  
292 Transmission is integrated across the wavelength band, and weighted by relative sensor response  
293 (RSR) (Barnes et al., 1998; Xiaoxiong et al., 2005) within the band. Because air mass factor ( $G^i$ )  
294 varies with gas type (on account of the vertical profile), LBLRTM calculates  $G^i$  as well as  
295 transmission for the given column amount of gas  $i$ . For “dry gas”, the integrated RSR weighted  
296 transmission is converted to gas optical depth, so dry gas transmission (as a function of air mass  
297 factors) is easily computed using Eq (1). The US 1976 Standard Atmosphere (US 76) profiles are  
298 used to compute “dry gas” transmission for nadir view.

299 Figure 3 plots the relationship between absorption correction factor,  $\tilde{T}_\lambda^{GAS}$ , and gas path  
300 length,  $G^{H_2O} w$ , for H<sub>2</sub>O (panel a) and,  $G^{O_3} O$ , for O<sub>3</sub> (panel b), for MODIS. Figure 4 plots the  
301 same for VIIRS. These correction factors (inverse of transmission) are plotted for each window  
302 band, for different combinations of H<sub>2</sub>O or O<sub>3</sub> concentrations ( $w$  in cm or  $O$  in DU) and  
303 internally derived air mass factors ( $G^i$ ) for the given gas type and specific vertical profile. For  
304 water vapor (panels (a) in both figures), a near-linear dependence of  $\tilde{T}_\lambda^{H_2O}$  to  $G^{H_2O} w$  exists in log-  
305 log space. Water vapor, being so variable as well as concentrated near the boundary layer, cannot  
306 be explained with a linear relationship. Even within the log-log space, there is small curvature  
307 that requires a quadratic for the empirical fit. For ozone, however, the log of our correction factor  
308 ( $\tilde{T}_\lambda^{O_3}$ ) is nearly linear as a function of absorption through a slant path ( $G^{O_3} O$ ). Again, note that  $G^i$   
309 is computed by LBLRTM, and represents the curvature and vertical profile of each gas type.



310 Equation 5 describes the quadratic empirical relationship (seen in Fig.3a and Fig 4a)  
 311 between gas transmission correction factor of water vapor ( $\tilde{T}_\lambda^{H_2O}$ ), its concentration ( $w$ ) and air  
 312 mass factor ( $G^{H_2O}$ ):

313

$$\tilde{T}_\lambda^{H_2O} = \exp(\exp(K_{1,\lambda}^{H_2O} + K_{2,\lambda}^{H_2O} \ln(G^{H_2O}w) + K_{3,\lambda}^{H_2O} (\ln(G^{H_2O}w))^2)) \dots \dots \dots (5)$$

314

315 and Equation 6 describes the near linear relationship for ozone (panels b in both Fig. 3  
 316 and Fig. 4).

317

$$\tilde{T}_\lambda^{O_3} = \exp(K_{1,\lambda}^{O_3} + K_{2,\lambda}^{O_3}(G^{O_3}O)) \dots \dots \dots (6)$$

318 “ $O$ ” denotes ozone concentration in Eq. 6 and  $G^i$  is the airmass factor for gas  $i$  and is  
 319 computed using equation 3.

320 The regression coefficients  $K_{1,\lambda}^{H_2O}$ ,  $K_{2,\lambda}^{H_2O}$ ,  $K_{3,\lambda}^{H_2O}$  and  $K_{1,\lambda}^{O_3}$ ,  $K_{2,\lambda}^{O_3}$  (the slopes and intercepts)  
 321 for H<sub>2</sub>O and O<sub>3</sub> are presented for MODIS and VIIRS in Tables 3.1 and Table 3.2. The slope and  
 322 intercepts are wavelength dependent (lines of different color on Figs. 3 and 4) and in accordance  
 323 to absorption characteristics of the gas. For example Table 2.1 shows that water vapor absorption  
 324 is highest in MODIS band 7 (B7 = 2.11 μm) and lowest in B3 (0.47 μm). Correspondingly, the  
 325 slope and intercept for the H<sub>2</sub>O regression relation (Table 3.1) indicates largest water vapor  
 326 correction in B7 and lowest in B3. Similarly, largest correction (and slope) for ozone is in  
 327 MODIS B4 (0.55 μm) and lowest in B7.





328 To calculate the correction factors for water vapor ( $\tilde{T}_\lambda^{H_2O}$ ) and ozone ( $\tilde{T}_\lambda^{O_3}$ ), Equations (5)  
 329 and (6) require information on water vapor ( $w$ ) and ozone concentration ( $O$ ). For the DT  
 330 algorithm, these are provided by an ancillary data set. For the current version (e.g. MODIS  
 331 Collection 6), ancillary data are acquired from National Center for Environmental Prediction  
 332 (NCEP) analysis, specifically the “PWAT” and the ozone fields from the  $1^\circ \times 1^\circ$  global  
 333 meteorological analysis (created every six hours – format “gdas.PGrbF00.YYMMDD.HHz”).  
 334 Note that there are water vapor products derived operationally from MODIS and VIIRS data  
 335 (e.g. Gao and Goetz, 1990; Kaufman and Gao, 1992). However, the DT aerosol algorithm runs  
 336 before these other algorithms in the processing chain, causing the internally-derived water vapor  
 337 to be unavailable to the aerosol algorithm in real-time processing and thus, the reliance on  
 338 ancillary data.

339 In case the ancillary information is not available, the gas absorption can still be estimated.  
 340 Either a forecast field (e.g. GDAS forecast) or a “climatology” can be used. For example, if the  
 341 US76 atmosphere is assumed as the climatology for gas profiles, then  $\tau^i$  for that gas is given in  
 342 Table 3.1 and 3.2. In this case, we use Equations (7) and (8) to calculate correction factors for  
 343 water vapor and ozone respectively:

$$\tilde{T}_\lambda^{H_2O} = \exp(G^{H_2O} \overline{\tau^{H_2O}}) \quad \dots \dots \dots (7)$$

$$\tilde{T}_\lambda^{O_3} = \exp(G^{O_3} \overline{\tau^{O_3}}) \quad \dots \dots \dots (8)$$

344 where  $\overline{\tau^{H_2O}}$  and  $\overline{\tau^{O_3}}$  are the climatological mean values of gas optical depth for water vapor  
 345 and ozone, respectively.

346  $\tilde{T}_\lambda^{Dry Gas}$  is the correction factor due to dry gas, which includes CO<sub>2</sub>, CO, N<sub>2</sub>O, NO<sub>2</sub>, NO,  
 347 CH<sub>4</sub>, O<sub>2</sub>, SO<sub>2</sub>, other trace gases. Since the gases are generally well-mixed throughout the entire  
 348 atmosphere and do not experience day to day changes, we only consider the climatological mean



349 of the total optical depth of the combined dry gases, and compute its transmittance factor as  
 350 follows:

$$\tilde{\tau}_{\lambda}^{Dry\ Gas} = \exp(G^i \overline{\tau^{Dry\ Gas}}) \dots \dots \dots (9)$$

351

352 Fig. 5 presents the gas optical depth for a US76 atmosphere, for the MODIS bands and  
 353 corresponding VIIRS bands. In some cases, (e.g. B4 vs. M5) the differences are small. In other  
 354 cases (e.g. B5 vs. M8), the total optical depth may be similar, but the relative contribution  
 355 between different gases different. Finally, in at least one set of bands (B7 vs. M11), both the total  
 356 optical depth and the relative contributions between gases is very different. The US76 is a case  
 357 of a small amount of water vapor ( $w=1.4$  cm), but one can see how quadrupling the  $w$  (e.g. as in  
 358 a tropical atmosphere) would greatly change the relative correction needed for B7 vs. M11, or  
 359 even B1 vs. M5.

360

### 361 3.3 Application within the DT algorithm.

362 Whether using “climatology” for water vapor and ozone columns, or using the estimates  
 363 from a meteorological assimilation system (e.g. GDAS for the current DT algorithm), we need to  
 364 correct for the combined absorption of all gases. The total gas absorption correction term,  $\tilde{\tau}_{\lambda}^{gas}$ ,  
 365 is the product of individual gas corrections, that is

$$\tilde{\tau}_{\lambda}^{gas} = \tilde{\tau}_{\lambda}^{H_2O} \tilde{\tau}_{\lambda}^{O_3} \tilde{\tau}_{\lambda}^{Dry\ Gas} \dots \dots \dots (10)$$

366 The MODIS DT aerosol retrieval algorithm ingests calibrated and geolocated MODIS-  
 367 measured reflectance data, known as the Level 1B (L1B) product. The corresponding VIIRS DT  
 368 algorithm ingests a similar VIIRS-measured product. This measured reflectance,  $(\rho_{\lambda}^{L1B})$ , is



369 corrected for atmospheric water vapor, ozone and dry gas, using the correction factors derived  
370 above for each wavelength band:

$$\rho_{\lambda} = \tilde{T}_{\lambda}^{gas} \rho_{\lambda}^{L1B} \dots \dots (11)$$

371 where  $\rho_{\lambda}$  is the corrected or brightened reflectance that will now match the calculated TOA  
372 reflectances of the LUT, as described in Section 2.2. Note that this spectral reflectance  $\rho_{\lambda}$ ,  
373 represents the combination of Rayleigh (molecular scattering), plus aerosol in the atmosphere. It  
374 also includes contributions from Earth's surface (land or water).

375 The gas-absorption correction methodology is the same whether performed for MODIS  
376 or VIIRS. In fact, the equations (Eqs 5-11) have remained the same throughout all versions of  
377 the DT algorithm. As our ability to characterize absorption lines as well as the spectral response  
378 of the sensor has improved, it is the coefficients of the equations that have evolved. When the  
379 DT algorithm was updated from Collection 5 (C5) to Collection 6 (C6), the underlying gas  
380 absorption corrections became more sophisticated (Levy et al., 2013). This is represented in  
381 Table 4. The primary differences between C5 and C6 are that HITRAN database in LBLRTM is  
382 used in C6 instead of the MODTRAN parameterization available in 6S that was used in C5, and  
383 that additional "dry" gases have been included in C6's correction. These changes made a  
384 difference. The latest version of aerosol data from DT is Collection 6.1 that uses the same gas  
385 absorption corrections as C6. As the DT algorithm is ported from MODIS to VIIRS data, the  
386 quality of gas correction will also make a difference.

#### 387 **4 Impact of new gas coefficients**

388 The DT retrieval is based on a LUT approach wherein the measured and modeled spectral  
389 reflectance is matched for inversion. Any change affecting the calculation of gas-corrected



390 spectral reflectance will subsequently affect the retrieved AOD. *Levy et al.*, [2013] showed the  
391 impact of using the updated atmospheric corrections on MODIS C6 AOD retrievals. This led to  
392 higher AODs globally. Over land (ocean), the 0.55  $\mu\text{m}$  global mean AOD differed by  $\sim 0.02$   
393 (0.007). The large ( $>0.02$  regionally) change over land was primarily due to a larger gas  
394 correction in the 1.24  $\mu\text{m}$  MODIS B5 band (see *Levy et al.*, 2013; Fig. A2), which in turn  
395 increased the reflectance in B5, and subsequent estimate of the NDVI in the SWIR channels (B5  
396 vs. B7) used to estimate surface reflectance in other bands (*Levy et al.*, 2010). The stronger gas  
397 correction in B5 came from including the  $\text{O}_2$  absorption, which had not been accounted for in C5  
398 (see Table 2.1). Interestingly, *Levy et al.* [2013] noted that while the overall correction in B7  
399 (2.11  $\mu\text{m}$ ) remained similar, the relative weightings of “dry gas” and  $\text{H}_2\text{O}$  was revised.

400 Even though MODIS and VIIRS instruments have similar channels, the MODIS gas  
401 correction coefficients cannot be applied to aerosol retrievals from VIIRS observations. The  
402 slight differences in the bandwidth and channel’s central wavelengths (See Fig. 5) will  
403 compromise the accuracy of aerosol retrievals. For example, as compared with MODIS B7 (2.11  
404  $\mu\text{m}$ ), the VIIRS M11 (2.25  $\mu\text{m}$ ) band has less absorption from  $\text{H}_2\text{O}$ . However, MODIS B7 lies in  
405 a  $\text{CO}_2$  absorption band, while VIIRS M11 lies in a region of  $\text{CH}_4$  absorption. Although the  $\text{CH}_4$   
406 optical depth in VIIRS M11 is small ( $\sim 0.03$ ), it will affect the dark-target retrievals in the same  
407 way as  $\text{O}_2$  inclusion affected C6 retrievals (when compared to C5).

408 As a perturbation experiment we intentionally apply the MODIS gas corrections to the  
409 VIIRS observations, even though we know this to be incorrect. Figure 6a plots the spatial  
410 distribution of spectral TOA reflectance after applying VIIRS-appropriate gas corrections. It  
411 shows the mean monthly TOA reflectance for VIIRS. Figure 6b are the reflectance differences



412 between applying VIIRS-appropriate gas corrections and MODIS gas corrections to VIIRS  
413 observations. From top to bottom, we find a mean difference of 0%, -0.5%, -6.6%, -2.7%, -  
414 1.5%, 3.2% and 5.3% respectively in VIIRS channels M3, M4, M5, M7, M8, M10, M11.  
415 Looking back at Fig. 5, one can see that that for example, by using proper M5 assumptions  
416 instead of the B1 MODIS assumptions, we now apply only about half the correction as before,  
417 resulting in a 6.6% reduction of reflectance. Channel M7, with about 50% less water vapor  
418 correction (see Fig. 5), results in 2.7% lower reflectance. Larger gas corrections owing to CO<sub>2</sub>  
419 absorption in M10 and CH<sub>4</sub> absorption in M11 (Fig. 5), result in positive bias in M10 and M11  
420 reflectance values globally.

421 Now, we continue the perturbation experiment and test the impact of slight differences in  
422 the band positioning between MODIS and VIIRS on AOD retrieval by performing two sets of  
423 retrievals. The first set (a) is if we applied appropriate VIIRS band corrections, while the second  
424 (b) is as if we had simply (naively) applied MODIS (C6) coefficients to VIIRS data. Figure 7  
425 shows the AOD retrieved from these two cases (panels a and b) for an entire month (July 2013)  
426 of VIIRS data. While general AOD spatial patterns are in agreement, panel (c) shows differences  
427 in AOD of up to 0.07 between the two retrievals. Clearly, naively applied MODIS gas  
428 corrections to VIIRS data, would lead to a global mean AOD underestimate of ~0.01 for July  
429 2013. While these differences are within the global uncertainties for AOD (e.g. GCOS), the  
430 regional differences can be much larger.

431 Although once considered to be trivial in magnitude, accurate atmospheric gas  
432 corrections have become more important as we strive towards better accuracies in AOD products  
433 and towards a seamless climate data record. It is noteworthy that the gas absorption spectra of  
434 Figure 1 have been updated several times in recent years [Alvarado et al. 2012] as the scientific



435 community continues to engage in study of gas absorption lines with improved instrumentation  
436 and gas spectroscopic measurements. Changing gas absorption spectra will affect the channels  
437 designed for new remote sensing instruments and in understanding how these lines might affect  
438 the retrieval of proposed geo-physical products. Every instrument design involves  
439 characterization of channel bandwidths and the spectral response functions of the instrument's  
440 channels. This aptly calls for updates in modeling the absorption by gases in the channels used  
441 for aerosol retrievals. For the MODIS Collection 6 AOD product, the team switched from using  
442 a MODTRAN gas spectroscopic database to the HITRAN spectroscopic database and found  
443 differences.

#### 444 **5. Summary and Conclusions**

445 Performing aerosol optical depth retrieval, from satellite measurements, requires  
446 extracting the aerosol signal from the total radiance measured by the sensor at the top-of-  
447 atmosphere. The total radiance includes signal from the underlying surface and from atmospheric  
448 constituents such as gases, clouds and aerosols. In this paper, we have described the physics and  
449 methodology employed by the Dark-Target aerosol retrieval algorithm for atmospheric gas  
450 correction of the cloud-free radiance measurements from the MODIS and VIIRS sensors. We  
451 have shown that the empirical correction applied to one sensor (MODIS) cannot be applied to  
452 another sensor (VIIRS) even when the channels of the two sensors may be similar. For a specific  
453 month of VIIRS observations (July, 2013), not accounting for the sensor's bandwidth and  
454 positioning of its central wavelength in the electro-magnetic spectrum, can result in an AOD  
455 retrieval bias of about 0.01 (global average) and up to 0.07 at regional scales.



456 Water vapor, ozone and carbon dioxide are the major absorbers of solar radiation.  
457 Historically, they have been accounted for in atmospheric gas corrections by aerosol retrieval  
458 algorithms. However, until recently, standard routine algorithms (e.g. the DT algorithm used on  
459 MODIS) did not consider other gases. For example, oxygen with a gas optical depth of about  
460 0.016 is important in the MODIS Band 5 (1.24  $\mu\text{m}$ ) [Levy et al., 2013]. Methane is an important  
461 absorber in band M11 (2.25  $\mu\text{m}$ ) of VIIRS with an optical depth of  $\sim 0.05$ . Starting with MODIS  
462 Collection 6, and the DT algorithm ported to VIIRS, seven additional atmospheric gases [CO,  
463 N<sub>2</sub>O, NO<sub>2</sub>, NO, CH<sub>4</sub>, O<sub>2</sub>, SO<sub>2</sub>] are addressed by the gas correction in these DT algorithms.

464 For the ‘dry gas’ component, the DT gas correction assumes a homogeneous global  
465 distribution spatially and a US76 type of vertical distribution for the eight gases. Carbon dioxide,  
466 oxygen, nitrous oxide and methane are major absorbers in our ‘dry gas’ category. Except for  
467 NO<sub>2</sub>, which is highly variable in both horizontal and vertical, the other gases tend to be well-  
468 mixed throughout the atmosphere. Spatial variability of well-mixed gases is typically around  
469 10%, mostly latitudinal and is smaller than seasonal variability (e.g. see methane maps here:  
470 <http://www.temis.nl/climate/methane.html>). For nadir view, 10% error due to spatial variability  
471 will only introduce an error of 0.005 in the methane correction (optical depth  $\sim 0.05$  in VIIRS  
472 channel M11). For now, this is a small uncertainty in the overall retrieval. However, as  
473 requirements for aerosol retrieval accuracies tighten, even these well-mixed dry gases will  
474 require removal of any seasonal and regional biases by using ancillary measurements of these  
475 gases or at least seasonal global climatology of gas optical depths, instead of a single  
476 climatological value for the entire globe.

477 Since the DT algorithm corrects for H<sub>2</sub>O and O<sub>3</sub> using ancillary data at every 1° X 1° grid  
478 box, spatial and seasonal variability of these gases is being accounted for. However, the ancillary



479 data has its own uncertainties that propagate into the gas correction and aerosol retrieval. The  
480 Dark-Target team is working towards estimating the error in per-pixel AOD retrievals introduced  
481 from several error sources including the errors in H<sub>2</sub>O and O<sub>3</sub> ancillary data (GDAS) used for  
482 atmospheric gas corrections. Preliminary analysis suggests (not shown here) that gas corrections  
483 errors, stemming from considering 20% errors in ancillary data, are much smaller (more than an  
484 order of magnitude) than errors from surface albedo uncertainty, aerosol model selection, spatial  
485 heterogeneity in a scene, calibration and cloud contamination errors. This is work in progress and  
486 subject to future publication.

487         The VIIRS instrument onboard Suomi-NPP is a follow-on of the MODIS instrument on  
488 Terra and Aqua satellites. While the Dark-Target team strives to create a seamless climate data  
489 record (CDR) of AOD from MODIS and VIIRS, it requires a consistency in AOD retrieval of  
490 about 0.02. Any compromise with the accuracy of AOD retrieved from either sensor will impact  
491 the CDR consistency requirement. To strive toward these requirements, we cannot ignore quality  
492 atmospheric gas corrections in AOD retrievals and we will update the gas correction factors for  
493 each instrument as the community updates the gas absorption database.

494         As we move into an era of new aerosol missions, revisiting and updating atmospheric  
495 corrections in state-of-art algorithm becomes as important as improving upon other factors (e.g.  
496 better surface characterization, cloud clearing, aerosol properties etc.) that affect the AOD  
497 retrieval. The dark-target algorithm software has now been generalized to retrieve AOD from  
498 sensors other than MODIS and VIIRS. It will be necessary to accurately characterize gases from  
499 such current and future instruments as Himawari, GOES-R, etc.

500

501







503 **Acknowledgements**

504 This research work is funded under NASA's grants for MODIS and VIIRS Dark Target  
505 aerosol retrieval for the MODIS science team. We are thankful to Matthew J. Alvarado (from  
506 Atmospheric and Environmental Research) for promptly helping with all our queries related to  
507 the LBLRTM. We thank Pubu Ciren for providing us with the atmospheric profiles for gases and  
508 for knowledge transfer on its use in LBLRTM for calculating NOAA VIIRS atmospheric gas  
509 corrections in aerosol retrievals  
510

511  
512

513 **References**

514

515 Anderson, G.P., A. Berk, P.K. Acharya, L.S. Bernstein, S.M. Adler-Golden, J. Lee, and L.  
516 Muratov, "Reformulated Atmospheric Band Model Method for Modeling Atmospheric  
517 Propagation at Arbitrarily Fine Spectral Resolution and Expanded Capabilities," U.S. Patent  
518 #7593835, issued September 22, 2009.

519

520 Berk, A., G.P. Anderson, P.K. Acharya, L.S. Bernstein, L. Muratov, J. Lee, M. Fox, S.M. Adler-  
521 Golden, J.H. Chetwynd, M.L. Hoke, R.B. Lockwood, J.A. Gardner, T.W. Cooley, C.C. Borel,  
522 P.E. Lewis and E.P. Shettle, "MODTRAN5: 2006 Update," Proc. SPIE, Vol. 6233, 62331F,  
523 2006.

524

525 Berk, A., P.K. Acharya, L.S. Bernstein, G.P. Anderson, P. Lewis, J.H. Chetwynd, M.L. Hoke,  
526 "Band Model Method for Modeling Atmospheric Propagation at Arbitrarily Fine Spectral  
527 Resolution," U.S. Patent #7433806, issued October 7, 2008.

528

529 Boucher, O., D. Randall, P. Artaxo, C. Bretherton, G. Feingold, P. Forster, V.-M. Kerminen, Y.  
530 Kondo, H. Liao, U. Lohmann, P. Rasch, S.K. Satheesh, S. Sherwood, B. Stevens and X.Y.  
531 Zhang, 2013: Clouds and Aerosols. In: Climate Change 2013: The Physical Science Basis.  
532 Contribution of Working Group I to the Fifth Assessment Report of the Intergovernmental Panel  
533 on Climate Change [Stocker, T.F., D. Qin, G.-K. Plattner, M. Tignor, S.K. Allen, J. Boschung,  
534 A. Nauels, Y. Xia, V. Bex and P.M. Midgley (eds.)]. Cambridge University Press, Cambridge,  
535 United Kingdom and New York, NY, USA.

536

537 Charlson, R.J., S.E. Schwartz, J.M. Hales, R.D. Cess, J.A. Coakley, Jr., J.E. Hansen, and D.J.  
538 Hoffman, 1992: Climate forcing by anthropogenic aerosols. *Science*, **255**, 423-430,  
539 doi:10.1126/science.255.5043.423.

540

541 Clough, S. A., Iacono, M. J., and Moncet, J.-L.: Line-by-Line calculations of atmospheric fluxes  
542 and cooling rates: application to water vapor, *J. Geophys. Res.-Atmos.*, **97**, 15761,  
543 doi:10.1029/92JD01419, 1992.

544 Clough, S. A., Shephard, M. W., Mlawer, E. J., Delamere, J. S., Iacono, M. J., Cady-Pereira, K.,  
545 Boukabara, S., and Brown, P. D.: Atmospheric radiative transfer modeling: a summary of the  
546 AER codes, *J. Quant. Spectrosc. Ra.*, **91**, 233–244, doi:10.1016/j.jqsrt.2004.05.058, 2005.

547 Denman, K. L., et al., 2007: Couplings between changes in the climate system and  
548 biogeochemistry. In: Climate Change 2007: The Physical Science Basis. Contribution of  
549 Working Group I to the Fourth Assessment Report of the Intergovernmental Panel on Climate  
550 Change [Solomon, S., D. Qin, M. Manning, Z. Chen, M. Marquis, K. B. Averyt, M. Tignor and  
551 H. L. Miller (eds.)] Cambridge University Press, Cambridge, United Kingdom and New York,  
552 NY, USA, pp. 499- 587.

553 Deuzé, J. L., M. Herman, P. Goloub, D. Tanré, and A. Marchand, "Characterization of  
554 aerosols over ocean from POLDER/ADEOS-1", *Geophys. Res. Lett.*, **26**:10 (1999),  
555 1421–1424.



- 556 Gao, B. C., and Alexander F. H. Goetz, Column Atmospheric Water Vapor and Vegetation  
557 Liquid Water Retrievals From Airborne Imaging Spectrometer Data, *J. Geophys. Res.*, 95, 3549-  
558 3564, 1990.  
559
- 560 Gao, B.-C., Y. J. Kaufman, D. Tanré, and R.-R. Li, 2002: Distinguishing tropospheric aerosols  
561 from thin cirrus clouds for improved aerosol retrievals using the ratio of 1.38- $\mu\text{m}$  and 1.24- $\mu\text{m}$   
562 channels. *Geophys. Res. Lett.*, **29**, 1890, doi:10.1029/2002GL015475.  
563
- 564 GCOS: Systematic observation requirements for satellite-based products for climate, 2011 up-  
565 date, WMO GCOS Rep. 154, New York, USA, 127 pp., 2011.
- 566 Gueymard, C.: SMARTS2: a simple model of the atmospheric radiative transfer of sunshine:  
567 algorithms and performance assessment, Florida Solar Energy Center, 1–78, 1995.
- 568 Heggin, M.I. et al. (2014): “Twenty questions and answers about the ozone layer: 2014  
569 Update”, in Scientific Assessment of Ozone Depletion: 2014. *World Meteorological  
570 Organization Global Ozone Research and Monitoring Project - Report No. 55*. Available from  
571 NOAA ESRL at  
572 <http://www.esrl.noaa.gov/csd/assessments/ozone/2014/twentyquestions/>  
573
- 574 Herman, J. R., P. K. Bhartia, O. Torres, C. Hsu, C. Seftor, and E. Celarier, “Global distribution  
575 of UV-absorbing aerosols from Nimbus 7/TOMS data”, *J. Geophys. Res.*, 102  
576 (1997), 16,911–16,922.
- 577 Higurashi, A., and T. Nakajima, “Development of a two channel aerosol retrieval algorithm  
578 on global scale using NOAA AVHRR”, *J. Atmos. Sci.*, 56 (1999), 924–941.
- 579 Hollmann, R., Merchant, C. J., Saunders, R., Downy, C., Buchwitz, M., Cazenave, A., Chu-  
580 vieco, E., Defourny, P., de Leeuw, G., Forsberg, R., Holzer-Popp, T., Paul, F., Sandven, S.,  
581 Sathyendranath, S., van Roozendaal, M., and Wagner, W.: The ESA Climate Change Initia-  
582 tive: satellite data records for essential climate variables, *B. Am. Meteorol. Soc.*, 94, 1541–  
583 1552, doi:10.1175/BAMS-D-11-00254.1, 2013.
- 584 Kahn, R., P. Banerjee, and D. McDonald, “The sensitivity of multiangle imaging to natural  
585 mixtures of aerosols over ocean”, *J. Geophys. Res.*, 106 (2001), 18,219–18,238.
- 586 Kaufman, Y. J., and B.-C. Gao, Remote sensing of water vapor in the near IR from  
587 EOS/MODIS, *IEEE Trans. Geosci. Remote Sensing*, 30, 871-884, 1992.  
588
- 589 Kaufman, Y. J., D. Tanré, L. A. Remer, E. F. Vermote, A. Chu, and B. N. Holben, “Operational  
590 remote sensing of tropospheric aerosol over land from EOS moderate resolution imaging  
591 spectroradiometer”, *J. Geophys. Res.*, 102, D14 (1997a), 17,051–17,067.  
592
- 593 Kaufman, Y. J., A. E. Wald, L. A. Remer, B.-C. Gao, R.-R. Li, and L. Flynn, 1997b: The MODIS 2.1  
594  $\mu\text{m}$  Channel - Correlation with visible reflectance for use in remote sensing of aerosol. *IEEE Trans.  
595 Geo*, **35**, 1286-1298.  
596



- 597 Kaufman, Y. J., Remer, L. A., Tanré, D., Li, R.-R., Kleidman, R. G., Mattoo, S., Levy, R., Eck, T.,  
598 Holben, B. N., Ichoku, C., Martins, J. V. and Koren, I.: A critical examination of the residual cloud  
599 contamination and diurnal sampling effects on MODIS estimates of aerosol over ocean., *IEEE Trans.*  
600 *Geosci. Remote Sens.*, **43**, 2886-2897, 2005.
- 601  
602 Knapp, K. R., T. H. Vonder Haar, and Y. J. Kaufman, “Aerosol optical depth retrieval from  
603 GOES-8: Uncertainty study and retrieval validation over South America”, *J. Geophys.*  
604 *Res.*, 107, D7 (2002), 4055, doi: 10.1029/2001JD000505.
- 605  
606 Lenoble, J., L.A. Remer and D. Tanré: *Aerosol Remote Sensing*, Springer, Heidelberg-New  
607 York-Dordrecht-London, 390 pp., ISBN 978-3-642-17724-8, 2013.
- 608  
609 Levy, R. C., Mattoo, S., Munchak, L. A., Remer, L. A., Sayer, A. M., Patadia, F., and Hsu, N.  
610 C.: The Collection 6 MODIS aerosol products over land and ocean, *Atmos. Meas. Tech.*, 6,  
611 2989-3034, <https://doi.org/10.5194/amt-6-2989-2013>, 2013.
- 612  
613 Levy, R. C., Munchak, L. A., Mattoo, S., Patadia, F., Remer, L. A., and Holz, R. E.: Towards a  
614 long-term global aerosol optical depth record: applying a consistent aerosol retrieval algorithm to  
615 MODIS and VIIRS-observed reflectance, *Atmos. Meas. Tech.*, 8, 4083-4110,  
616 <https://doi.org/10.5194/amt-8-4083-2015>, 2015.
- 617  
618 Li, R.-R., Remer, L., Kaufman, Y. J., Mattoo, S., Gao, B.-C. and Vermote, E.: Snow and ice mask for  
619 the MODIS aerosol products., *IEEE Geosci Rem. Sens. Lett.*, **2**, 306-310, 2005.
- 620  
621 Lim, S. S., et al. (2012), A comparative risk assessment of burden of disease and injury  
622 attributable to 67 risk factors and risk factor clusters in 21 regions, 1990?2010: a systematic  
623 analysis for the Global Burden of Disease Study 2010, *The Lancet*, 380(9859), 2224-2260.
- 624  
625 Liu, Z., A. H. Omar, Y. Hu, M. A. Vaughan, and D. M. Winker, CALIOP Algorithm  
626 Theoretical Basis Document Part 3: Scene Classification Algorithms, PC-SCI-202 Part  
627 3, NASA Langley Research Center, Hampton VA, 2005.
- 628  
629 Martins, J. V., D. Tanré, L. A. Remer, Y. J. Kaufman, S. Mattoo and R. Levy , 2002: MODIS Cloud  
630 Screening for Remote Sensing of Aerosol over Oceans using Spatial Variability. *Geophys. Res. Lett.*,  
631 **29(12)**, 10.1029/2001GL013205, 2002.
- 632  
633  
634 Martonchik, J. V., D. J. Diner, R. A. Kahn, T. P. Ackerman, M. E. Verstraete, B. Pinty, and  
635 H. R. Gordon, “Techniques for the retrieval of aerosol properties over land and ocean  
636 using multiangle imaging”, *IEEE Trans. Geosci. Rem. Sens.*, 36 (1998), 1212–1227.
- 637  
638 McCormick, M. P., P. Hamill, T. J. Pepin, W. P. Chu, T. J. Swissler, and L. R. McMaster,  
639 “Satellite studies of the stratospheric aerosol”, *Bull. Am. Meteorol. Soc.*, 60 (1979),  
640 1038–1046.
- 641



- 642 Rothman, L. S., et al. (2009), The HITRAN 2008 molecular spectroscopic database, *J. Quant.*  
643 *Spectrosc. Radiat. Transfer*, 110, 533–572
- 644
- 645 Sayer, A. M., N. C. Hsu, C. Bettenhausen, Z. Ahmad, B. N. Holben, A. Smirnov, G. E. Thomas,  
646 and J. Zhang (2012), SeaWiFS Ocean Aerosol Retrieval (SOAR): Algorithm, validation, and  
647 comparison with other data sets, *J. Geophys. Res.*, 117, D03206, doi:[10.1029/2011JD016599](https://doi.org/10.1029/2011JD016599).
- 648
- 649 Starr, D. et al.: 2010: Aerosol, Clouds and Ecosystems (ACE) Study Report. Submitted to  
650 NASA Headquarters June 2010.  
651 [https://acemission.gsfc.nasa.gov/documents/Draft\\_ACE\\_Report2010%20.pdf](https://acemission.gsfc.nasa.gov/documents/Draft_ACE_Report2010%20.pdf)
- 652
- 653 Stowe, L. L., A. M. Ignatov, and R. R. Singh, “Development, validation, and potential  
654 enhancements to the second-generation operational aerosol product at the National  
655 Environmental Satellite, Data, and Information Service of the National Oceanic and  
656 Atmospheric Administration”, *J. Geophys. Res.*, 102 (1997), 16,923–16,934.
- 657
- 658 Tanré, D., B.N. Holben and Y.J. Kaufman, 1992: Atmospheric correction algorithm for  
659 NOAA-AVHRR products: theory and application. *IEEE Trans. Geosci. Rem. Sens.*, 30, 231 –  
660 248, doi:[10.1109/36.134074](https://doi.org/10.1109/36.134074).
- 661
- 662 Tanré, D., Y. J. Kaufman, M. Herman, and S. Mattoo, “Remote sensing of aerosol properties  
663 over oceans using the MODIS/EOS spectral radiances”, *J. Geophys. Res.*, 102: D14  
664 (1997), 16,971–16,988.
- 665
- 666 Thomas, G. E., Poulsen, C. A., Siddans, R., Sayer, A. M., Carboni, E., Marsh, S. H., Dean, S.  
667 M., Grainger, R. G., and Lawrence, B. N.: Validation of the GRAPE single view aerosol retrieval  
668 for ATSR-2 and insights into the long term global AOD trend over the ocean, *Atmos. Chem.*  
669 *Phys.*, 10, 4849–4866, <https://doi.org/10.5194/acp-10-4849-2010>, 2010.
- 670
- 671 Torres, O., P. K. Bhartia, J. R. Herman, Z. Ahmad, and J. Gleason, “Derivation of aerosol  
672 properties from satellite measurements of backscattered ultraviolet radiation: Theoretical  
673 basis”, *J. Geophys. Res.*, 103 (1998), 17,099–17,110.
- 674
- 675 U.S. Standard Atmosphere, 1976, U.S. Government Printing Office, Washington, D.C., 1976
- 676
- 677 Veefkind, J. P., G. de Leeuw, and P. A. Durkee, “Retrieval of aerosol optical depth over  
678 land using two–angle view satellite radiometry during TARFOX”, *Geophys. Res. Lett.*,  
679 25:16 (1998), 3135–3138.
- 680
- 681 Vermote, E. F., D. Tanré, J. L. Deuzé, M. Herman, and J. J. Morcrette, “Second simulation of the  
682 satellite signal in the solar spectrum, 6S: An overview”, *IEEE Trans. Geosci. Rem. Sens.*, 35  
683 (1997), 675–686.
- 684
- 685 W. L. Barnes, T. S. Pagano, V. V. Salomonson, "Pre-launch characteristics of the Moderate  
686 Resolution Imaging Spectroradiometer (MODIS) on EOS AM-1", *IEEE Trans. Geosci. Remote*  
687 *Sens.*, vol. 36, no. 4, pp. 1088–1100, Jul. 1998.



688  
689 Xiaoxiong Xiong, Nianzeng Che and W. Barnes, "Terra MODIS on-orbit spatial characterization  
690 and performance," in *IEEE Transactions on Geoscience and Remote Sensing*, vol. 43, no. 2, pp.  
691 355-365, Feb. 2005.  
692 doi: 10.1109/TGRS.2004.840643  
693  
694 Z. Ahmad, C. McClain, J. Herman, B. Franz, E. Kwiatkowska, W. Robinson, E. Bucsele, and M.  
695 Tzortziou, "Atmospheric correction for NO<sub>2</sub> absorption in retrieving water-leaving reflectances  
696 from the SeaWiFS and MODIS measurements," *Appl. Opt.* 46, 6504-6512 (2007).  
697  
698  
699  
700  
701  
702  
703  
704  
705  
706  
707  
708  
709  
710  
711  
712  
713  
714  
715  
716  
717  
718  
719  
720  
721 **Figures**



722

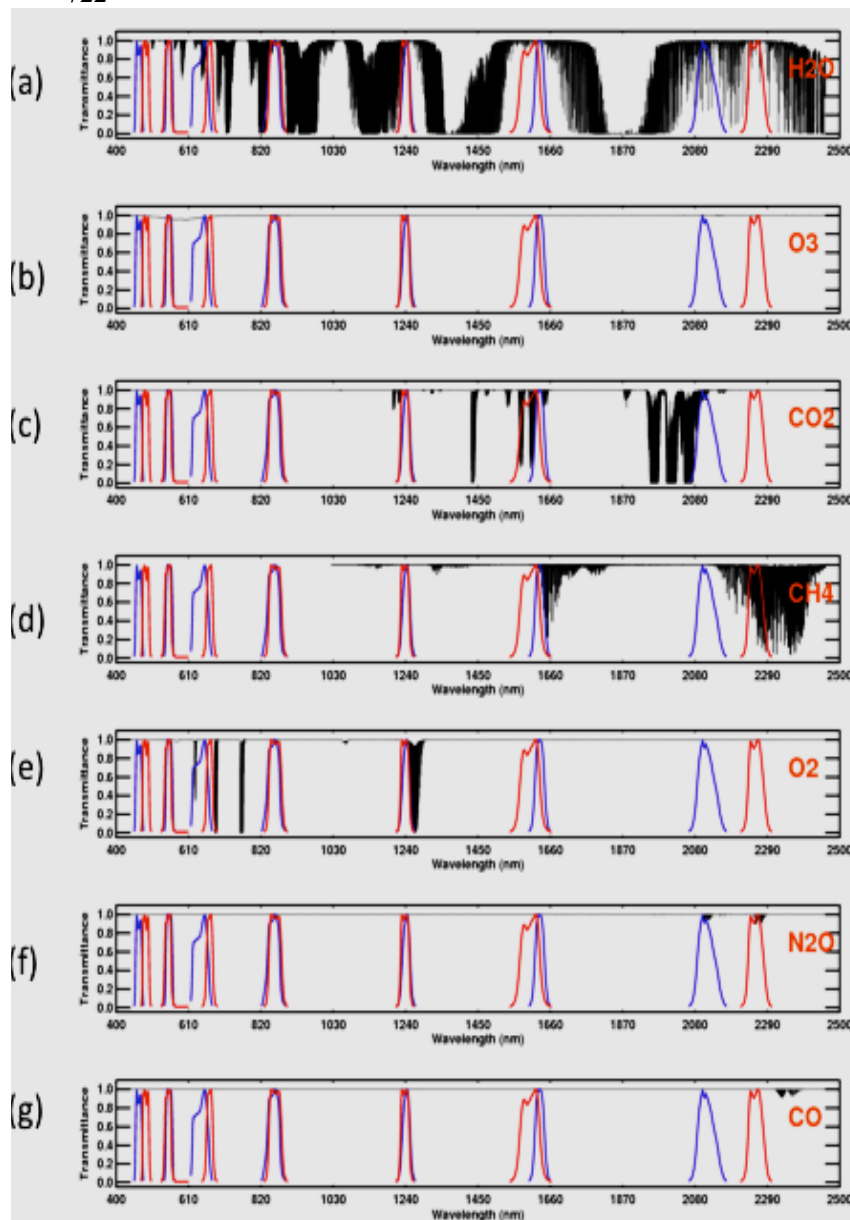


Figure 1

The TOA Transmission spectra (black) of the major atmospheric gases in the Visible and Near Infrared part of electromagnetic spectrum (400 – 2500 nm). The Line-by-line radiative transfer model (LBLRTM) was used to calculate these gas spectra for a nadir viewing geometry and the 1976 US Standard atmosphere. The spectral response functions of MODIS channels B1-B7 (blue curves) and seven VIIRS channels (red curves) are overlaid for visualizing their positioning in atmospheric ‘window’ region where gas absorption effect is minimal

723  
724  
725  
726  
727  
728  
729





730  
731  
732

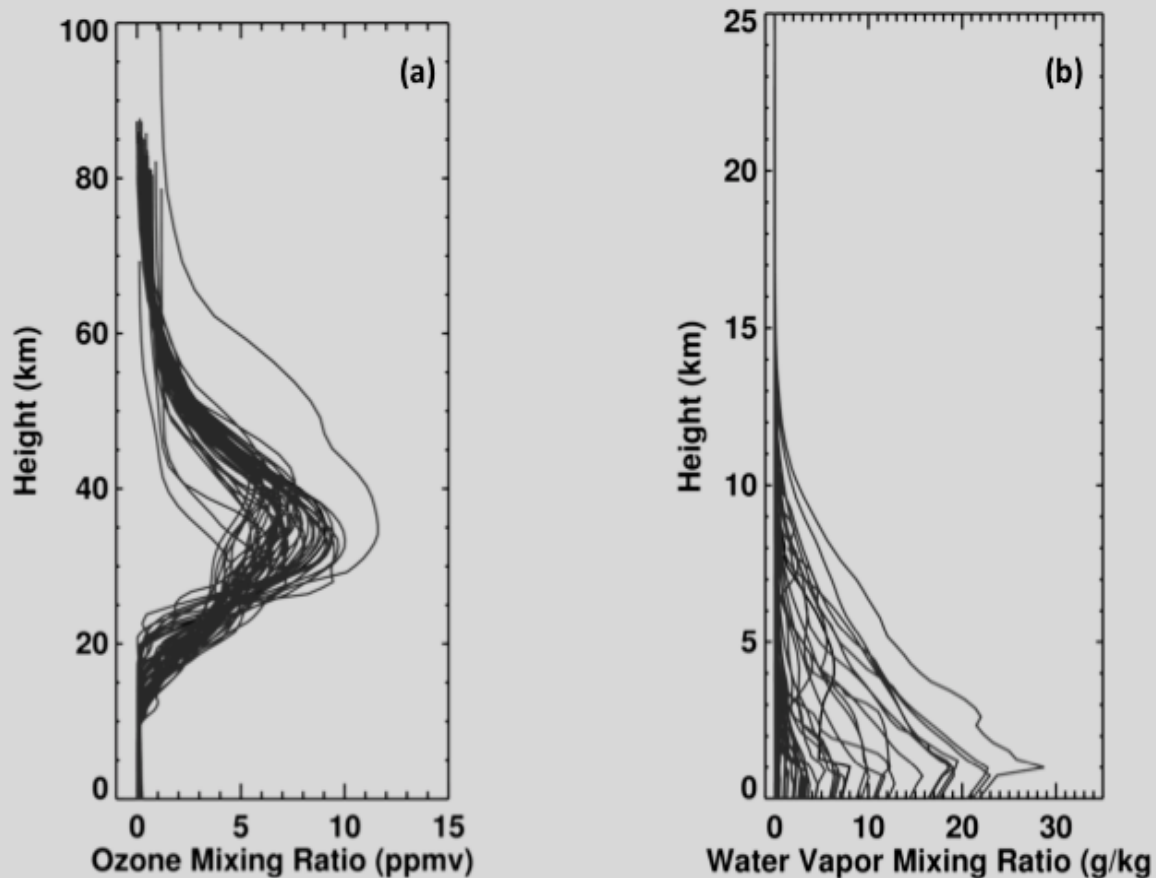
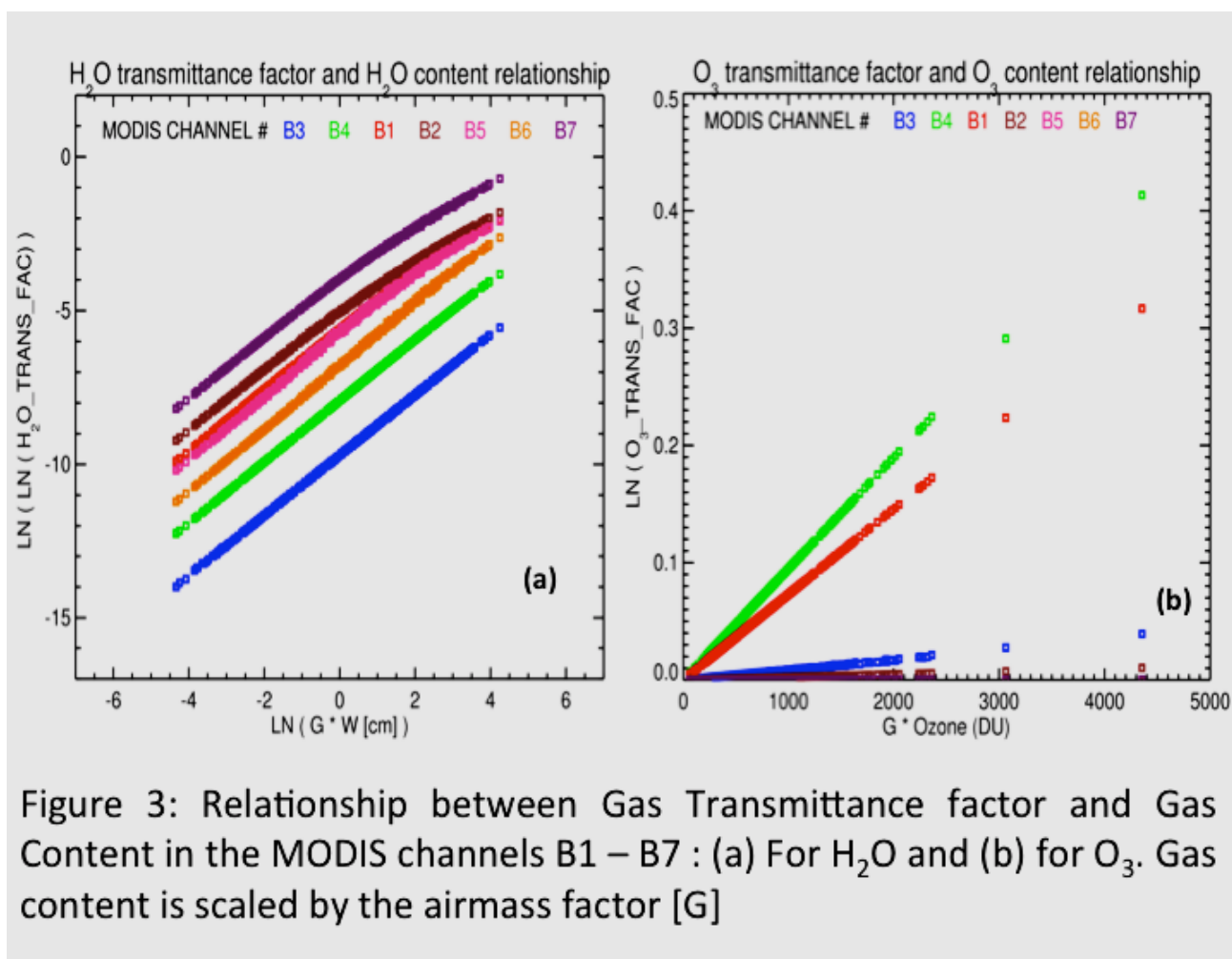


Figure 2: 52 different ECMWF profiles for (a) water vapor and (b) ozone used in the Line-by-line radiative transfer model to calculate the respective gas transmittance.

733  
734  
735  
736  
737  
738  
739  
740



741



742  
743  
744  
745  
746  
747  
748  
749  
750  
751  
752  
753



754

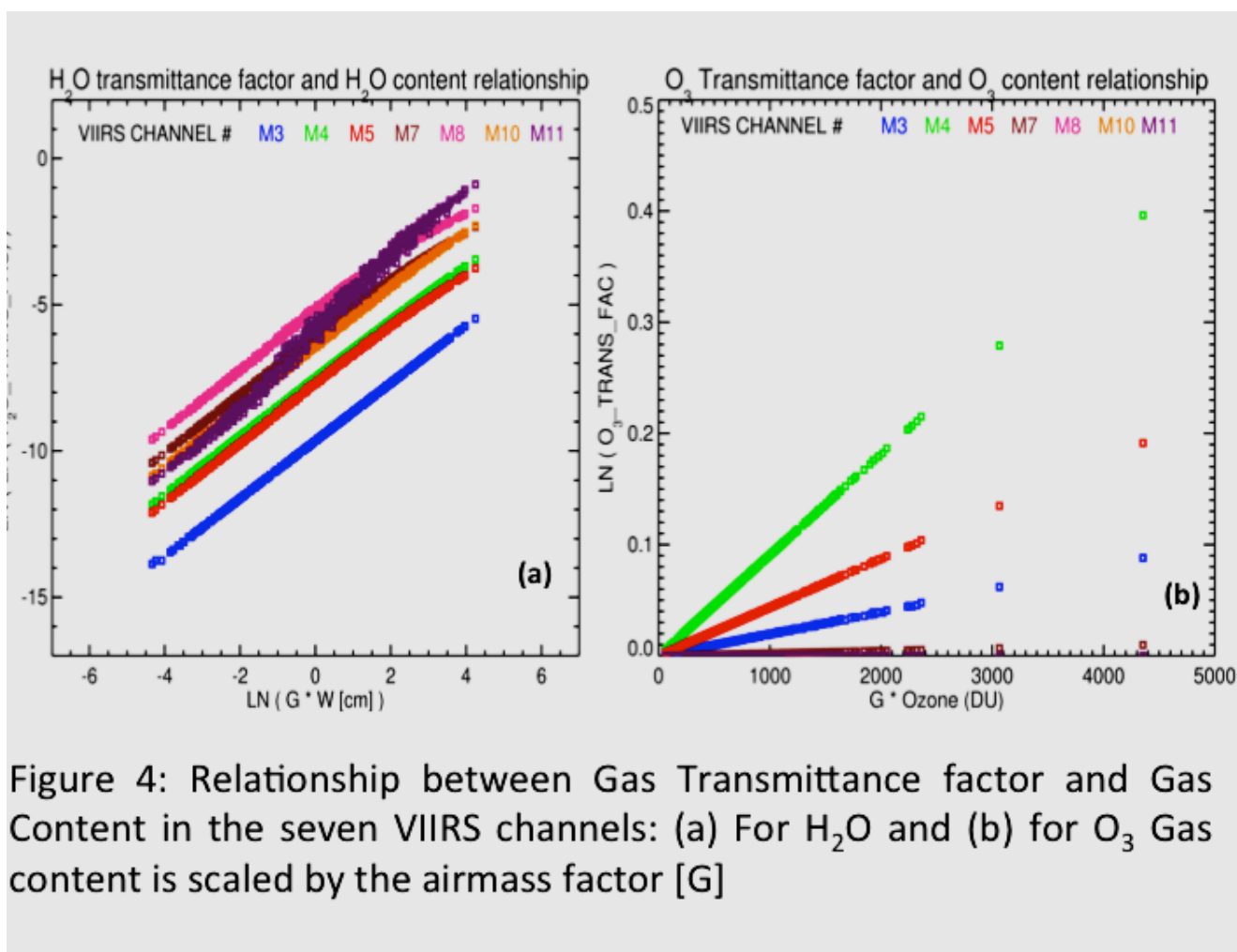


Figure 4: Relationship between Gas Transmittance factor and Gas Content in the seven VIIRS channels: (a) For H<sub>2</sub>O and (b) for O<sub>3</sub> Gas content is scaled by the airmass factor [G]

755  
756  
757  
758  
759  
760  
761  
762  
763  
764  
765  
766  
767



768  
 769

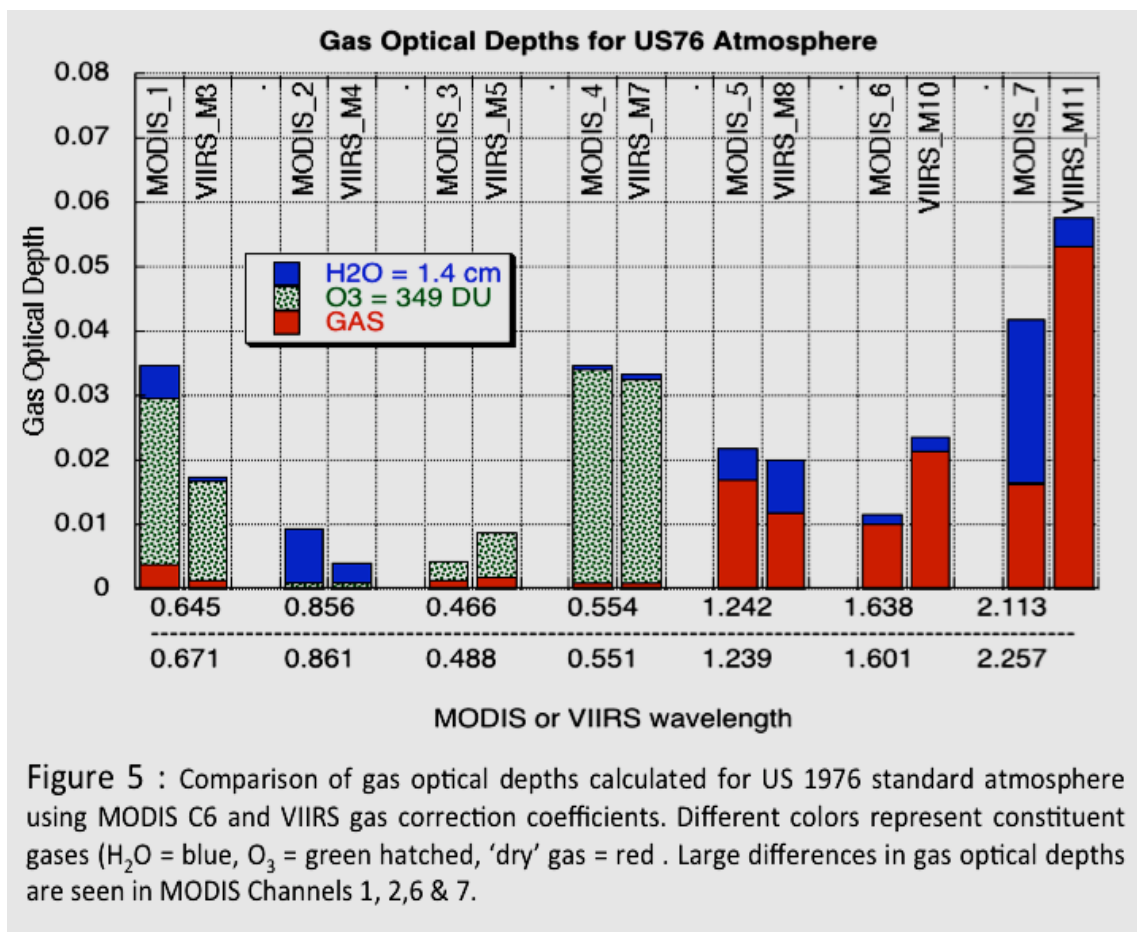


Figure 5 : Comparison of gas optical depths calculated for US 1976 standard atmosphere using MODIS C6 and VIIRS gas correction coefficients. Different colors represent constituent gases (H<sub>2</sub>O = blue, O<sub>3</sub> = green hatched, 'dry' gas = red). Large differences in gas optical depths are seen in MODIS Channels 1, 2, 6 & 7.

770  
 771  
 772  
 773  
 774  
 775  
 776  
 777  
 778  
 779  
 780  
 781  
 782  
 783  
 784



785

### VIIRS Reflectance

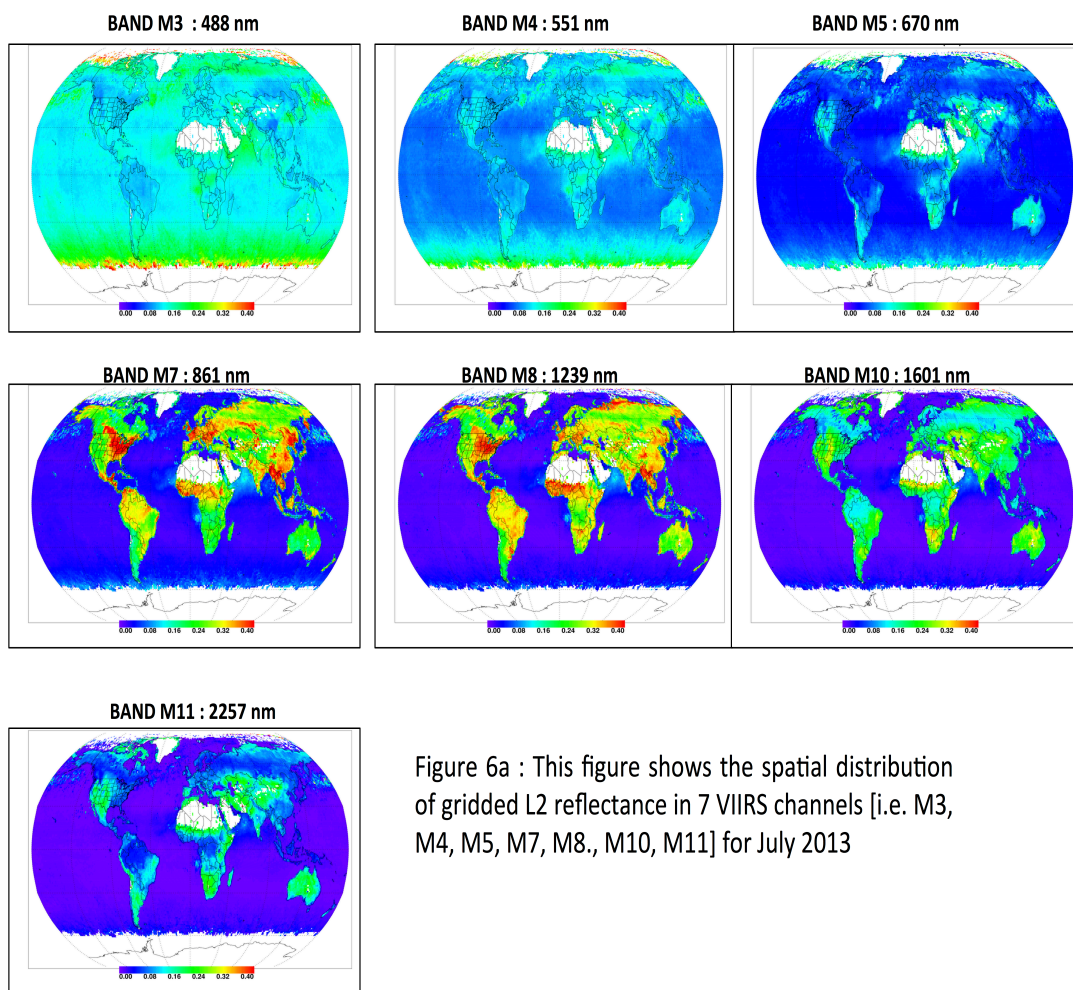


Figure 6a : This figure shows the spatial distribution of gridded L2 reflectance in 7 VIIRS channels [i.e. M3, M4, M5, M7, M8., M10, M11] for July 2013

786  
787  
788  
789  
790  
791



792  
793

### Difference between VIIRS – C6 Gas Reflectance

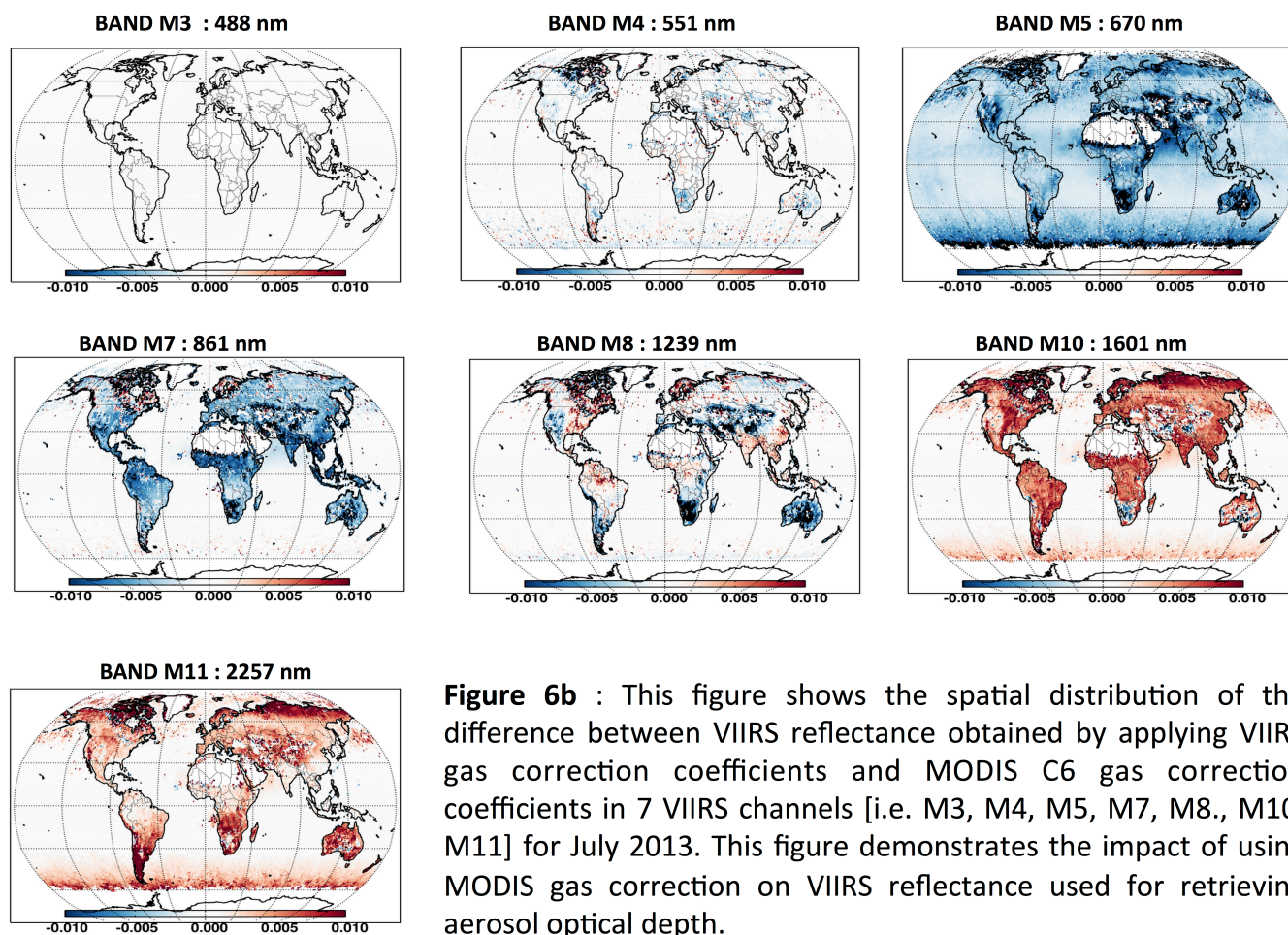
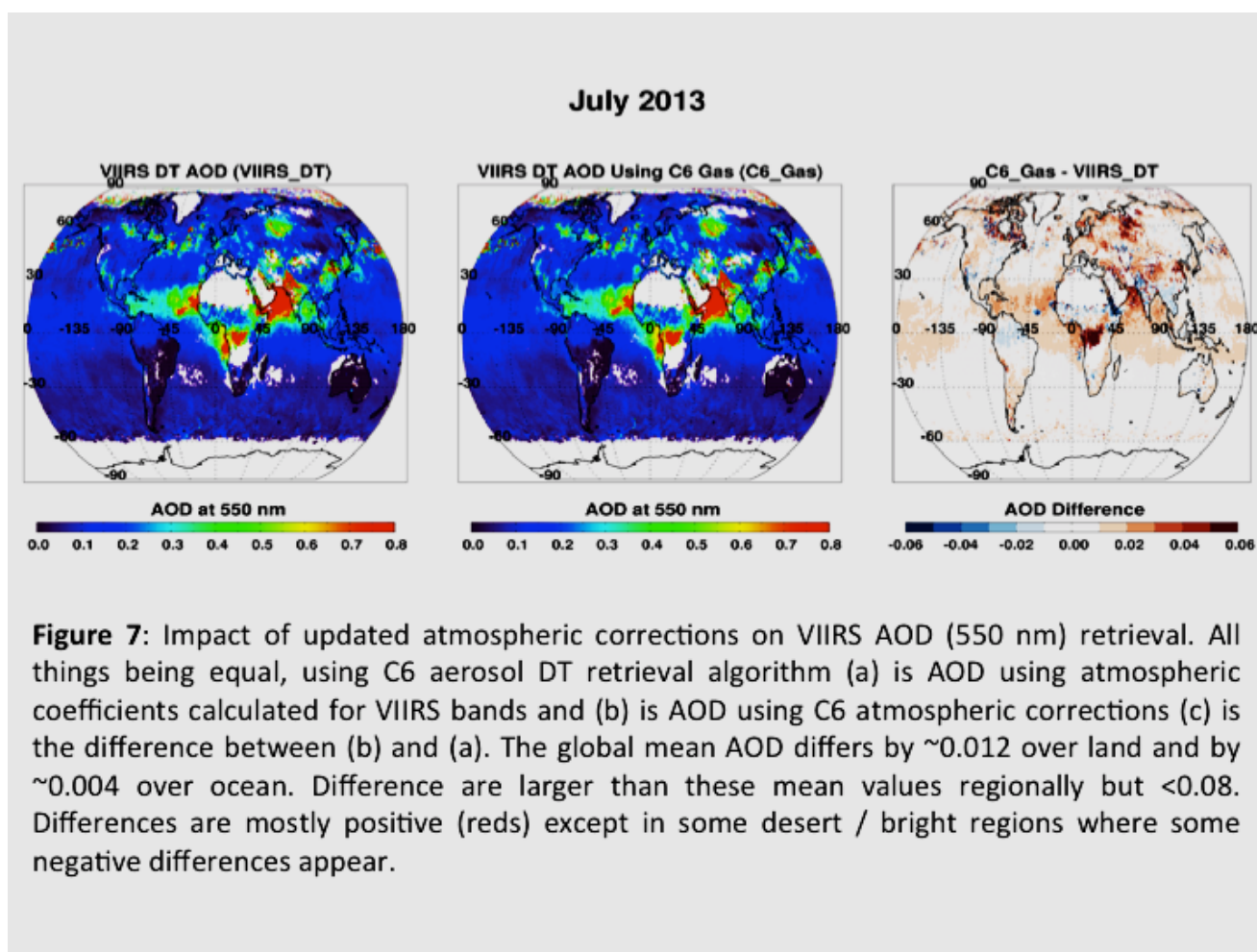


**Figure 6b** : This figure shows the spatial distribution of the difference between VIIRS reflectance obtained by applying VIIRS gas correction coefficients and MODIS C6 gas correction coefficients in 7 VIIRS channels [i.e. M3, M4, M5, M7, M8., M10, M11] for July 2013. This figure demonstrates the impact of using MODIS gas correction on VIIRS reflectance used for retrieving aerosol optical depth.

794  
795  
796  
797  
798  
799  
800  
801  
802  
803



804



805  
806  
807  
808  
809  
810  
811  
812  
813  
814  
815  
816  
817  
818



819 **Tables**  
 820

**Table 1 : Absorption bands of atmospheric gases in visible and near-IR region**

Major Atmospheric Gas	Center Wavelengths ( $\mu\text{m}$ )
$\text{H}_2\text{O}$	visible, 0.72, 0.82, 0.94, 1.1 1.38, 1.87, 2.7
$\text{CO}_2$	1.4, 1.6, 2.0, 2.7, 4.3
$\text{O}_3$	visible (0.45 - 0.75)
$\text{O}_2$	0.63, 0.69, 0.76, 1.06, 1.27, 1.58
$\text{N}_2\text{O}$	2.87, 4.06, 4.5
$\text{CH}_4$	1.66, 2.2, 3.3
$\text{CO}$	2.34, 4.67
$\text{NO}_2$	visible

821  
 822  
 823  
 824  
 825  
 826  
 827  
 828  
 829  
 830  
 831  
 832  
 833  
 834  
 835  
 836  
 837  
 838  
 839  
 840  
 841  
 842  
 843  
 844  
 845  
 846  
 847  
 848  
 849  
 850  
 851  
 852  
 853  
 854  
 855  
 856





857

**Table 2.1 : Optical depth of major atmospheric gases in 7 MODIS channels.**

858  
 859  
 860

Channel	B3	B4	B1	B2	B5	B6	B7
Wavelength ( $\mu\text{m}$ )	0.466	0.553	0.645	0.856	1.242	1.638	2.113
Gas							
H <sub>2</sub> O	0.0001	0.0005	0.0055	0.0086	0.005	0.0017	0.0254
O <sub>3</sub>	0.0029	0.0326	0.0250	0.0008	-	-	0.0000
CO <sub>2</sub>	-	-	-	-	0.0003	0.0050	0.0142
N <sub>2</sub> O	-	-	-	-	-	-	0.0020
CO	-	-	-	-	-	-	-
O <sub>2</sub>	0.0012	0.0010	0.0038	0.0000	0.0164	-	-
NO	-	-	-	-	-	-	-
SO <sub>2</sub>	-	-	-	-	-	-	-
NO <sub>2</sub>	-	-	-	-	-	-	-
CH <sub>4</sub>	-	-	-	-	0.0000	0.0051	0.0003
<b>Total</b>	<b>0.0042</b>	<b>0.0341</b>	<b>0.0344</b>	<b>0.0094</b>	<b>0.0216</b>	<b>0.0118</b>	<b>0.0420</b>

861  
 862

Highlighted boxes show channels where total gas optical depth  $\geq 0.02$  to put in context the requirement of aerosol optical depth accuracy of better than 0.02

863  
 864  
 865



866

**Table 2.2 : Optical depth of major atmospheric gases in 7 VIIRS channels**

867

Channel Gas	M3	M4	M5	M7	M8	M10	M11
Wavelength (µm)	0.488	0.551	0.67	0.861	1.239	1.601	2.257
Gas							
H2O	0.00009	0.00078	0.00066	0.00324	0.00844	0.00234	0.00542
O3	0.00673	0.0312	0.01499	0.00075	0	0	0
CO2	0	0	0	0	0.00041	0.02048	0.00001
N2O	0	0	0	0	0	0.00001	0.00403
CO	0	0	0	0	0	0	0
O2	0.00184	0.00084	0.00144	0.00002	0.01147	0	0
NO	0	0	0	0	0	0	0
SO2	0	0	0	0	0	0	0
NO2	0	0	0	0	0	0	0
CH4	0	0	0	0	0.00001	0.00085	0.04914
<b>Total</b>	<b>0.00866</b>	<b>0.03282</b>	<b>0.01709</b>	<b>0.00401</b>	<b>0.02033</b>	<b>0.02368</b>	<b>0.0586</b>

868

869

Highlighted boxes show channels where total gas optical depth  $\geq 0.02$  to put in context the requirement of aerosol optical depth accuracy of better than 0.02

870

871

872

873

874

875



**Table 3.1: Gas Absorption Coefficients and Climatology for MODIS**

MODIS Band	Wavelength ( $\mu\text{m}$ )	Rayleigh Optical Depth	O <sub>3</sub> Optical Depth <sup>#</sup>	H <sub>2</sub> O Optical Depth <sup>#</sup>	Dry Gas <sup>*</sup> Optical Depth <sup>#</sup>	O <sub>3</sub> _K0	O <sub>3</sub> _K1	H <sub>2</sub> O_K0	H <sub>2</sub> O_K1	H <sub>2</sub> O_K2
B3	0.4659	1.92E-01	2.90E-03	8.00E-05	1.25E-03	-1.14E-04	8.69E-06	-9.58E+00	1.23E+00	-1.16E-01
B4	0.5537	9.44E-02	3.26E-02	5.00E-04	9.50E-04	5.18E-06	9.50E-05	-7.91E+00	1.00E+00	-1.29E-02
B1	0.6456	5.08E-02	2.52E-02	5.11E-03	3.91E-03	1.16E-04	7.32E-05	-5.60E+00	9.40E-01	-1.78E-02
B2	0.8564	1.62E-02	8.10E-04	8.61E-03	2.00E-05	2.80E-07	2.36E-06	-5.07E+00	8.77E-01	-2.40E-02
B5	1.2417	3.61E-03	0.00E+00	5.23E-03	1.69E-02	1.19E-07	1.55E-25	-5.65E+00	9.81E-01	-2.38E-02
B6	1.6285	1.22E-03	0.00E+00	1.62E-03	9.98E-03	1.19E-07	5.17E-26	-6.80E+00	1.03E+00	-4.29E-03
B7	2.1134	4.30E-04	2.00E-05	2.53E-02	1.63E-02	6.29E-07	7.03E-08	-3.98E+00	8.86E-01	-2.56E-02

\* Dry Gas includes CO<sub>2</sub>, CO, N<sub>2</sub>O, NO<sub>2</sub>, NO, CH<sub>4</sub>, O<sub>2</sub>, SO<sub>2</sub>

# For each MODIS band, this nadir looking (viewing zenith angle = 0) optical depth for the gas is computed from the US 1976 Standard Atmosphere in LBLRTM.

876  
 877  
 878  
 879  
 880  
 881  
 882  
 883  
 884  
 885



886  
 887

**Table 3.2: Gas Absorption Coefficients and Climatology for VIIRS**

VIIRS Band	Wavelength (μm)	Rayleigh Optical Depth	O <sub>3</sub> Optical Depth <sup>#</sup>	H <sub>2</sub> O Optical Depth <sup>#</sup>	Dry Gas* Optical Depth <sup>#</sup>	O <sub>3</sub> _K0	O <sub>3</sub> _K1	H <sub>2</sub> O_K0	H <sub>2</sub> O_K1	H <sub>2</sub> O_K2
M3	0.488	1.60E-01	6.73E-03	8.94E-05	1.84E-03	-1.25E-04	1.98E-05	-9.65E+00	9.87E-01	1.80E-04
M4	0.5511	9.76E-02	3.11E-02	7.69E-04	8.34E-04	-4.75E-05	9.08E-05	-7.50E+00	9.84E-01	-3.87E-03
M5	0.6704	4.40E-02	1.50E-02	6.64E-04	1.44E-03	-4.79E-05	4.37E-05	-7.69E+00	9.95E-01	-1.10E-02
M7	0.8612	1.60E-02	7.70E-04	3.37E-03	2.45E-05	4.18E-07	2.24E-06	-6.05E+00	9.65E-01	-1.53E-02
M8	1.2389	3.67E-03	0.00E+00	8.44E-03	1.19E-02	1.19E-07	5.17E-26	-5.16E+00	9.59E-01	-2.67E-02
M10	1.6012	1.32E-03	0.00E+00	2.34E-03	2.13E-02	1.19E-07	1.03E-25	-6.43E+00	1.02E+00	-3.60E-03
M11	2.257	3.50E-04	1.07E-06	5.42E-03	5.32E-02	-2.61E-08	3.28E-09	-5.85E+00	1.28E+00	-5.04E-03

\* Dry Gas includes CO<sub>2</sub>, CO, N<sub>2</sub>O, NO<sub>2</sub>, NO, CH<sub>4</sub>, O<sub>2</sub>, SO<sub>2</sub>

# For each VIIRS band, this nadir looking (viewing zenith angle = 0) optical depth for the gas is computed from the US 1976 Standard Atmosphere in LBLRTM.

888  
 889  
 890  
 891  
 892  
 893  
 894  
 895



**Table 4: Atmosphere Gas Correction Table Differences : C5 vs C6**

	C5	C6	Comment
RT Code	6s	LBLRTM (Line-by-Line Radiative Transfer Model)	6S is MODTRAN (Ref) database LBLRTM is HITRAN (Ref) database
# Gases Considered	3 [H <sub>2</sub> O, O <sub>3</sub> , CO <sub>2</sub> ]	10 [H <sub>2</sub> O, O <sub>3</sub> , O <sub>2</sub> , CO, CO <sub>2</sub> , CH <sub>4</sub> , NO, N <sub>2</sub> O, NO <sub>2</sub> , SO <sub>2</sub> ]	Inclusion of 'other' dry gases in C6 created big differences in MODIS bands 5 & 7 (See Fig. 2)
Climatological GODs	Mid-latitude-Summer	US76 Standard Atmosphere	Ref
Rayleigh OD	Calculated for MODIS Bands's Fiter Function weighted Central $\lambda$ (Sensor centroid)	Calculated for TOA centroid $\lambda$ (solar irradiance and FF weighted)	Characteristic $\lambda$ changes slightly
	ROD calculated based on single characteristic wavelength	ROD integrated over filter function	Corresponding slight change in sea level ROD